



HAL
open science

Deformation and cavitation at the spherulite scale of semi-crystalline polymers

Lucien Laiarinandrasana, Olga Klinkova, Cristian Ovalle, Peter Cloetens, Thilo F. Morgeneyer

► **To cite this version:**

Lucien Laiarinandrasana, Olga Klinkova, Cristian Ovalle, Peter Cloetens, Thilo F. Morgeneyer. Deformation and cavitation at the spherulite scale of semi-crystalline polymers. 2023. hal-04100630v1

HAL Id: hal-04100630

<https://hal.science/hal-04100630v1>

Preprint submitted on 17 May 2023 (v1), last revised 7 Sep 2023 (v2)





HAL is a multi-disciplinary open access archive for the deposit and dissemination of scientific research documents, whether they are published or not. The documents may come from teaching and research institutions in France or abroad, or from public or private research centers.

L'archive ouverte pluridisciplinaire **HAL**, est destinée au dépôt et à la diffusion de documents scientifiques de niveau recherche, publiés ou non, émanant des établissements d'enseignement et de recherche français ou étrangers, des laboratoires publics ou privés.



Distributed under a Creative Commons Attribution 4.0 International License

Deformation and cavitation at the spherulite scale of semi-crystalline polymers

 Lucien Laiarinandrasana¹, Olga Klinkova²,  Cristian Ovalle¹,  Peter Cloetens³, and  Thilo F. Morgeneyer¹

¹ Mines Paris, PSL University, Centre for Material Sciences (MAT), UMR7633 CNRS, 91003 Evry, France

² Quartz laboratory EA7393, Supmeca Paris, 3 Rue Fernand Hainaut, F-93400 Saint-Ouen, France

³ European Synchrotron Radiation Facility (ESRF), BP 220, F-38043 Grenoble Cedex, France

Tensile tests on semi-crystalline thermoplastics generate engineering stress-strain curves, which may exhibit non linearity and/or peak stress associated with a striction/necking of the specimen at the macroscopic scale. This work addresses this state of deformed specimen where irreversible strains lead to a variable cross section area along the necked region. Using Synchrotron Radiation Computed Tomography with two high resolutions, 3D images in this region were exploited. The best resolution (1 pixel length = 0.05 μ m) allowed a better understanding of the morphology of several deformed spherulites within which polar fans arrangement was clearly detailed. For 0.7 μ m resolution, the longitudinal and transverse elongations of larger number of spherulites were measured. The evolution of the volumetric plastic strain due to cavitation at the spherulitic scale along the necked region was comprehensively analyzed. Volume change at this scale was highlighted, consisting of increase in the case of void growth followed by a decrease (compaction) at large strain due to the collapse of elongated voids. The effects of these results on the establishment of reliable constitutive model are discussed.

Keywords Semi-crystalline polymer, Spherulite, Cavitation, Deformation, Tomography

1 Introduction

In the nowadays requirement for sustainability and circular economy, the use of thermoplastic materials for engineering structures is one of the recommended solution due to their recyclability. To this end, investigation on the mechanical properties of these materials is a key point, whatever their origin: recycled or as initially processed. This work focuses on an isotactic polypropylene: a semi-crystalline thermoplastic with spherulitic microstructure [Laiarinandrasana et al., 2016b]. The aim is to relate the evolution of the microstructure, analyzed from 3D imaging technique, in terms of mechanisms of deformation and voiding, to the mechanical property allowing the constitutive relationship of the material to be established. The most common mechanical test dedicated to analyse the mechanical “behaviour” of a given material consists of a tensile loading applied to a smooth – therefore uniaxial – specimen. Generally, during such a test, a change in the specimen morphology (noted as necking or striction) [Ward, 1971],[Duffo et al., 1995], [Séguéla, 2007] appears when the yield stress is reached. This localisation of the deformation obviously introduces a heterogeneity within the gauge length of the specimen. This is accompanied by a change in the slope of the engineering stress-strain curve: non linearity, peak stress... This latter is considered as the manifestation at the macroscopic scale of a profound change at the microstructure scale [Blaise et al., 2010]. The spherulitic microstructure in its undeformed configuration (initial microstructure) is generally examined in 2D [Haudin, 2013],[Laiarinandrasana et al., 2016b], so as to evaluate the average diameter of the spherulite. In the recent years, tomography technique, especially Synchrotron Radiation Computed Tomography (SRCT) extended to 3D these examinations. One of the noticeable result [Selles et al., 2017], [Raphael et al., 2019], considered here as original, concerned 3D deformed spherulite in Polyamide 6, where the authors mentioned the existence of a cylindrical nucleus in the centre. Moreover, quantitative evaluation of the void volume fraction (porosity) through the thickness of smooth and notched round bars was performed by the authors [Laiarinandrasana et al., 2016b]. It was mentioned that whilst the spherulite axial deformation could easily be estimated by measuring the height of the polar fans [Pawlak and Galeski, 2008], [Pawlak and Galeski, 2010] in the tensile direction, the radial deformation was difficult to evaluate without a clear identification of the lateral boundary of these spherulites. Hence, this is the first objective of this paper, which could be attempted thanks to available SRCT data sets at two resolutions. A very good resolution at 0.05 μ m allowed the identification (learning) of 3D patterns of deformed shape of spherulites. A lower resolution of 0.7 μ m permitted more spherulites to be analyzed. Histograms of the height and the diameter of these spherulites were then plotted. The application of the continuum mechanics theory lays in the existence of a representative volume element (RVE). The authors mentioned [Laiarinandrasana et al., 2016b] that the initial rectangular cross section of the polypropylene under study became diamond like shaped during the tensile deformation. Indeed,

warping of the side of the cross section was systematically observed in 3D. After a clear definition of the RVE corresponding to the spherulitic microstructure, the effect of the aforementioned warping of the sides of the cross section was investigated as well. Addressing the mechanical properties, many attempts were made to access the local stress [Xiong et al., 2013] within the spherulite, by using the continuum mechanics framework. However, the only measurement available is the resulting force provided by the load cell i.e. at the macroscopic scale. The redistribution of this load to the three main directions of the space is guessed to be due to the microstructure. Therefore, estimating the local stresses requires reliable constitutive model which should be, at least, based on the strain measurements at the scale of the spherulite as mentioned above. In the literature, several models have been proposed for homogenized spherulite, beyond the yield stress i.e. during the necking process. The “plastic dilation” was taken into account by introducing the porosity as an internal variable in an approach using the mechanics of porous media ([Ognedal et al., 2014], [Laiarinandrasana et al., 2016a]... and references herein). Other models broke the homogenization assumption by considering an intrinsic stress-strain curve [Duffo et al., 1995],[Estevez et al., 2000],[Addiego et al., 2006],[Ponçot et al., 2013], clearly related to the ideally dense matrix, that is, responding to the deviatoric part of the stress and strain tensor. Several models even go further by distinguishing the crystalline and amorphous lamellae with their specific orientation inside the spherulite [van Dommelen et al., 2003], but without any mention about the voids observed in the considered spherulite. This paper aimed at shedding light to the aforementioned concepts, starting by a theoretical background on the continuum mechanics using the framework of total Lagrange finite strain formulation. The deformation gradient tensor will be considered as the input of the problem. The second section describes the investigated material together with the working methods and the tomographic data sets, at hand. The following section details the experimental results allowing the deformation gradient tensor to be obtained at three various scales, implying therefore, three RVEs’. In the last part, a discussion is set so as to propose the physical mechanisms underlying the deformation gradient components, in 3D, as well as the relevant constitutive models able to account for these mechanisms. This section ends by a short comment about the possible use of machine learning approach to handle big data available at the laboratory.

2 Theoretical background

In the framework of finite strain under total Lagrangian formulation, let $\underline{\underline{F}}$ be the deformation gradient in a cylindrical system of coordinates, with z being the tensile direction.

$$\underline{\underline{F}} = \begin{pmatrix} \lambda_r & 0 & 0 \\ 0 & \lambda_\theta & 0 \\ 0 & 0 & \lambda_z \end{pmatrix} \quad (1)$$

In the whole document, isotropy of the material is assumed, so that $\lambda_r = \lambda_{theta}$. Therefore, only two elongations will be considered:

- the longitudinal elongation λ_L which is equal to λ_z
- the transverse elongation $\lambda_T = \lambda_r = \lambda_\theta$

The simplified deformation gradient tensor which will be referred to in the following, becomes:

$$\underline{\underline{F}} = \begin{pmatrix} \lambda_T & 0 & 0 \\ 0 & \lambda_T & 0 \\ 0 & 0 & \lambda_L \end{pmatrix} \quad (2)$$

The classical multiplicative decomposition of $\underline{\underline{F}}$ writes:

$$\underline{\underline{F}} = \underline{\underline{F}}^e \underline{\underline{F}}^p = \begin{pmatrix} \lambda_T^e \lambda_T^p & 0 & 0 \\ 0 & \lambda_T^e \lambda_T^p & 0 \\ 0 & 0 & \lambda_L^e \lambda_L^p \end{pmatrix} \quad (3)$$

where superscripts e and p stand respectively for elastic and plastic components.

By using the logarithmic true strain measure, the strain tensor $\underline{\underline{\varepsilon}}$ can be deduced:

$$\underline{\underline{\varepsilon}} = \begin{pmatrix} \varepsilon_T = \ln(\lambda_T^e \lambda_T^p) & 0 & 0 \\ 0 & \varepsilon_T = \ln(\lambda_T^e \lambda_T^p) & 0 \\ 0 & 0 & \varepsilon_L = \ln(\lambda_L^e \lambda_L^p) \end{pmatrix} = \begin{pmatrix} \varepsilon_T^e + \varepsilon_T^p & 0 & 0 \\ 0 & \varepsilon_T^e + \varepsilon_T^p & 0 \\ 0 & 0 & \varepsilon_L^e + \varepsilon_L^p \end{pmatrix} \quad (4)$$

In this work, focus is put on $\underline{\underline{F}}^p$ which can be, in turn, multiplicatively splitted into its deviatoric $\underline{\underline{F}}_{dev}$ and volumetric $\underline{\underline{F}}_{vol}$ parts, by considering that

$$\underline{\underline{F}}_{dev} = J^{-1/3} \underline{\underline{F}} \quad (5)$$

where J is the jacobian of the transformation, equal to $\det(\underline{\underline{F}})$. J is constrained to keep the unity value for incompressible material.

$$\underline{\underline{F}}^P = \underline{\underline{F}}_{dev}^P \underline{\underline{F}}_{vol}^P = \begin{pmatrix} \lambda_{devT}^P \lambda_{volT}^P & 0 & 0 \\ 0 & \lambda_{devT}^P \lambda_{volT}^P & 0 \\ 0 & 0 & \lambda_{devL}^P \lambda_{volL}^P \end{pmatrix} \quad (6)$$

The true “plastic” strain tensor can be additively splitted as follows:

$$\underline{\underline{\varepsilon}}^P = \begin{pmatrix} \varepsilon_{devT}^P + \varepsilon_{volT}^P & 0 & 0 \\ 0 & \varepsilon_{devT}^P + \varepsilon_{volT}^P & 0 \\ 0 & 0 & \varepsilon_{devL}^P + \varepsilon_{volL}^P \end{pmatrix} \quad (7)$$

Conversely to the metallic materials, the originality is addressing the “plastic dilation” [Ognedal et al., 2014] *i.e.* the volumetric plastic strains. Knowing the whole strain tensor in eq. 7, constitutive relationships allow the complete local stress tensor to be determined. The approach consists of introducing the symmetric left Cauchy Green strain tensor $\underline{\underline{C}}$:

$$\underline{\underline{C}} = \underline{\underline{F}}^T \underline{\underline{F}} \quad (8)$$

where the superscript T deals with the transposition operation.

In virtue of eq. 5, it follows that:

$$\underline{\underline{C}}_{dev} = J^{-2/3} \underline{\underline{C}} \quad (9)$$

In addition, a deformation energy Ψ which is a particular case of the Helmholtz free energy is introduced, splitted also into an isochoric (Ψ_{iso}) and a volumetric (Ψ_{vol}) parts:

$$\Psi(\underline{\underline{C}}) = \Psi_{iso}(\underline{\underline{C}}_{dev}) + \Psi_{vol}(J) \quad (10)$$

The second stress tensor of Piola Kirschhoff $\underline{\underline{S}}$ can be derived from the deformation energy Ψ :

$$\underline{\underline{S}} = 2 \frac{\partial \Psi}{\partial \underline{\underline{C}}} = \underline{\underline{S}}_{vol} + \underline{\underline{S}}_{iso} \quad (11)$$

with:

$$\underline{\underline{S}}_{vol} = 2 \frac{\partial \Psi_{vol}(J)}{\partial \underline{\underline{C}}} = Jp \underline{\underline{C}}^{-1} = J^{1/3} \underline{\underline{C}}_{dev}^{-1} \quad (12)$$

where p is a Lagrange multiplier, and:

$$\underline{\underline{S}}_{iso} = 2 \frac{\partial \Psi_{iso}(\underline{\underline{C}}_{dev})}{\partial \underline{\underline{C}}} = J^{-2/3} \underline{\underline{P}} : \left[2 \frac{\partial \Psi_{iso}(\underline{\underline{C}}_{dev})}{\partial \underline{\underline{C}}_{dev}} \right] \quad (13)$$

with $\underline{\underline{P}}$ a fourth order projection tensor into tyhe deviatoric space, which can be expressed as:

$$\underline{\underline{P}} = \underline{\underline{I}} - \frac{1}{3} \underline{\underline{C}}^{-1} \otimes \underline{\underline{C}} = \underline{\underline{I}} - \frac{1}{3} \underline{\underline{C}}_{dev}^{-1} \otimes \underline{\underline{C}}_{dev} \quad (14)$$

$\underline{\underline{I}}$ being the fourth order identity tensor and \otimes operator defined as:

$$(\underline{\underline{A}} \otimes \underline{\underline{B}})_{ijkl} = A_{ij} B_{kl} \quad (15)$$

Once $\underline{\underline{S}}$ has been determined, the first Piola-Kirschhoff (engineering stress $\underline{\underline{\Pi}}$) and the Cauchy stress (true stress $\underline{\underline{\sigma}}$) tensors can be derived, following:

$$\underline{\underline{\Pi}} = J \underline{\underline{\sigma}} \underline{\underline{F}}^{-T} \quad (16)$$

$$\underline{\underline{\sigma}} = J^{-1} \underline{\underline{F}} \underline{\underline{S}} \underline{\underline{F}}^T \quad (17)$$

These first Piola-Kirschhoff and Cauchy stress tensors can also be splitted into their deviatoric and isostatic parts by applying the same transports as in eqs (16-17) to the stress tensor components in eq (12) and eq.(13), respectively. Furthermore, each stress tensor component is related to the corresponding deformation gradient. In particular, the volumetric component of the deformation gradient in eq. (6) or the strain tensor in eq (7) are directly related to the isostatic stress tensor. This work aims at determining the complete deformation gradient tensor (eq. (3)) and proposing a route to estimate, at the spherulitic scale, the local multiaxial Cauchy stress tensor (eq. (17)), from 3D measurements.

3 Material, methods and data sets

3.1 Semi-crystalline isotactic polypropylene

The material under study is a semi-crystalline isotactic polypropylene (PP) with a glass transition temperature $T_g = -7.9$ °C and an index of crystallinity $\chi = 47$ %, measured with the Modulated Differential Scanning Calorimetry (MDSC). Optical microscope examinations on microtomed slices of the rectangular section showed a skin-core effect, as detailed in [Laiarinandrasana et al., 2016b] and illustrated in figure 1a. This latter figure shows a through thickness cut from a microtomed thin layer of the PP material at a large scale. Some oriented stripes, corresponding to trans-crystalline zones [Kantz et al., 1972] [Assouline et al., 2001], were noticed. In the following, the presence of these zones was not accounted for, but several examinations at this scale allowed the determination of an average thickness of the skin layer of about 350 μm from the lateral free surfaces.

The present work focuses on the spherulites within the core. However, although spherulitic shapes could be distinguished in the core, from the viewgraph (fig. 1a), closer looks were required in some places (figures. 1b-c), so as to allow measurements of the spherulite diameters. Actually, the field of view was optimized so as to let the boundaries of the spherulite be well resolved in the micrograph.

From about 30 spherulites with clear morphology, the histogram of the measured diameters was plotted in figure 1d. They were observed to be rather equiaxial, with an average diameter of about 56 μm . This isotropy in the morphology and this initial value of the diameter are of crucial importance for the determination of the spherulitic strains when the specimen is stretched. Note that the minimum and maximum measured diameters were respectively 30 and 80 μm

3.2 Volumes of interest versus representative volume elements

As mentioned in [Laiarinandrasana et al., 2016b], dog bone ISO flat specimens, with a gauge length of 25 mm were used. They were tested at 20 °C and at a relative humidity of 50% thanks to an electromechanical tensile rig at various crosshead speeds. For the specific specimen that has been comprehensively analyzed here, the tensile test run until the plateau stress, after having experienced the peak stress and the stress softening.

The representative volume element (RVE) definition implies homogeneous (or homogenized) medium where the stress and the strain are homogeneous as well. At the macroscopic scale, two RVE were introduced, noted respectively as “skin” and “core”. The skin RVE was supposed to correspond to the gauge length, that is (25 mm \times 4 mm \times 2 mm). Note this skin RVE assumed a homogenized volume where the skin-core effects were ignored. By subtracting the skin thickness (about 0.7 mm), the core RVE was reduced to (25 mm \times 3.3 mm \times 1.3 mm). The core RVE was supposed to be composed of an ensemble of spherulites regardless the distribution of their sizes.

As soon as necking appeared, at the peak stress, these RVE contained a strain localization around the neck. In this region the stress and strain were expected to exhibit gradient and a triaxiality ratio. Here, the interest is to study the measured displacements/strains at three scales. The RVE was subdivided into VOI, which in turn, was reduced to focus on the three volumes in the necked region as illustrated in [Laiarinandrasana et al., 2016b]. These VOI's were examined with synchrotron radiation tomography/laminography technique at two resolutions for which 1 px, corresponded, respectively, to 0.7 μm [Laiarinandrasana et al., 2016a] and 50 nm [Morgeneyer et al., 2014]. Accordingly, three scales of VOI were analyzed: macroscopic at the surface (skin), at the level of the core and at the scale of the spherulite.

3.3 Data sets and metrology

As mentioned above, the present study attempts to analyze in detail a necked region. To this end, figure 2 recalls the three VOI's corresponding to tomographic data sets at a resolution of 0.7 μm . At the bottom of the figure, the selected cylindrical coordinates were sketched, where z , r and θ were associated with respectively the longitudinal, width and thickness directions. Note that r and θ directions may be called transverse direction meaning, respectively, through diametrical, width and thickness for spherulite and core/skin volumes. The scale is given at the bottom of figure 2 as well.

For the sake of clarity, it should be noted that:

- the figures 2a and b correspond respectively to side and top views of the three VOI's where VOI#3 (at the top) was the more necked region;
- the side views in fig. 2a correspond to mid-width virtual cut of the tomographic data set in 3D instead of the commonly used mid-thickness cut to see the neck through the width. Actually, the width was too large compared with the field of view of the synchrotron radiation tomography setup;
- experimental artifacts did not allow to obtain consecutive data sets, a VOI located between VOI#2 and VOI#3 is missing due to a failure of the reconstruction.

On fig. 2b, warping of the side was systematically observed especially on VOI#3 as commented in the figure. Therefore, the observation at mid-width corresponded to the minimum thickness when the sample

was deformed. Additionally, in each viewgraph, one can distinguish the skin and the core. As a matter of fact, the skin is more warped than the core, which cross section remained more rectangular.

From figure 2, characteristic lengths were deduced. To this end, fig. 3 plots the relative position of the VOIs' associated to the measured thicknesses. It should be mentioned that:

- the origin of the coordinate $z = 0$ is the bottom line of VOI#1;
- the total height of the studied deformed sample was 5.7 mm;
- The keys indicating VOI numbers were positioned at the barycentre of each VOI. Each measurement on the VOI will be displayed at the coordinate of its barycentre.

It can be observed that the thickness is not constant for each VOI, neither for the surface (skin) nor for the core of the sample. Nevertheless, the initial through thickness gauge length was the same; that is 1.3 mm and 2 mm, respectively, for the core and the "skin" (say macroscopic) sample.

At the microscopic scale, the deformed spherulites will be used as markers for the measurements of the deformation. After a comprehensive learning of 3D images, it turned out that, in figure 2b, the boundary of the spherulites was more discernible than in fig. 2a. A systematic study of the 3D-shape of deformed spherulites was then performed so as to obtain the longitudinal extension and the lateral contraction/dilation at two resolutions of Synchrotron Radiation Computed Tomography.

3.4 Deformed spherulites at a resolution of $0.7\mu\text{m}$

Fig. 4 displays various views in 3D of deformed spherulites at a resolution corresponding to $1\text{ px} = 0.7\mu\text{m}$. An attempt was made to volate one deformed spherulite in the centre of a cube with $140\mu\text{m}$ side (fig. 4a). From the side view in lateral cut of this cube, one can see polar fans [Pawlak and Galeski, 2008] composed of materials (light) and penny shaped voids (black) piled up in columns. This specific structure of double polar fans is generally admitted to be included inside a spherulite. However, whilst the polar fans are clearly shown, the boundary of the spherulite is not well resolved. [Laiarinandrasana et al., 2016b] suggested to determine the height of the deformed spherulite by measuring that of the polar fans. Note that in between the two polar fans (central region), is located the nucleus of the spherulite [Selles et al., 2017], [Raphael et al., 2019], where no void could be observed. In the top face of fig. 4a, circular voids are discernible meaning that the boundary of the spherulite should also be equi-axial.

Figure 4b shows a clip box of approximately $1/8$ of the cube, removed so as to display the microstructure in 3D inside the spherulite. The "north" polar fan of the spherulite is visible through the vertical line crossing the centre of the cube. The "south" polar fan is partially shown, the remainder being hidden by the "matter" let by the clip box. The boundary of the spherulite around the north polar fan is clearly visible. In addition, the top view let appear more or less dashed lines corresponding to the polygonal boundary of the spherulite. Actually the diameter is easier to determine from the top view.

By using Avizo software [refAvvol], surface rendering of the spherulite boundaries together with the polar fans was performed (fig. 4c). Again, the spherulites were so nested in the side view that it was difficult to obtain fair quantification of the characteristic distances (diameters and heights). A better resolution applied on few spherulites allowed to learn more about the details of these patterns. The nano-tomography (or holotomography) technique as used by [Morgeneyer et al., 2014] and [Ovalle et al., 2021] was utilized here, the resolution corresponding to $1\text{ px} = 50\text{ nm}$.

4 Results

4.1 Closer 3D examinations of deformed spherulites

The tomographic data set with a resolution corresponding to $1\text{ px} = 50\text{ nm}$ was selected in the centre of a necked region. This was composed of a cylindrical volume of $102.4\mu\text{m}$ in both diameter and height.

Figure 5 corresponds to the side views (longitudinal cut) of the nano-tomographic data set. The tensile direction being vertical according to this view. The polar fans already reported for various semi-crystalline polymers [Pawlak and Galeski, 2008, Pawlak and Galeski, 2010, Rozanski and Galeski, 2013] were the basic pattern from which the image recognition will be based in the following. In figure 5a, a couple of polar fans are highlighted with vertical dashed red arrows indicating their boundaries. Focusing first on the detail of the polar fans (right border of fig. 5a), it can be observed alternatively penny-shaped disks of voids and matters for which the diameter increased when away from the centre. It should however be noted that inside the voids some tranverse fibrils were observed and the disks were rather "curved" like spherical caps. Moreover, the cylindrical nucleus described by [Selles et al., 2017] and [Raphael et al., 2019] is clearly evidenced in between the north and the south polar fans.

Focusing on the second polar fans surrounded by the four vertical dashed red arrows located in the middle of fig. 5a, three voids having nucleated from nanometric rigid particles were indicated by horizontal red arrows. In particular, the void named as P#1 is located in the centre of the nucleus. These voids emanating from nanodefects (P#1, P#2 and P#3) are much smaller than those inside the polar fans. One can then conclude that critical voids are due to the spherulitic microstructure and not from nanoscopic defects

in the material.

From this side view and even at this resolution, again the boundaries of spherulites are not well resolved. Although the vertical red dashed arrows seem to indicate they are straight, it is easier to determine the total height of the polar fans and attribute this to that of the deformed spherulite.

Figure 5b displays the whole side view (longitudinal cut) of the nano-tomographic data set where three entire polar fans are visible together with four partial polar fans. Three spherulites named as Sph#1, Sph#2, Sph#3, were considered here.

- Sph #1: located in the top left of fig. 5b. Surrounded by a vertical dashed red rectangle, it was noticed that the nucleus contained more than seven voids having nucleated from rigid particles. The nucleus has therefore been extended much more than the others observed in the same data set;
- Sph #2: a nucleated void was noticed as well in the central region of the nucleus. Additionally, the south end of the polar fan is hidden probably by the forefront; meaning the polar fan may be slightly tilted. A vertical cut cannot show the whole polar fans inducing uncertainties on the measurement of the height of the spherulite;
- Sph #3: the south polar fan is clearly seen with discernible boundaries: the lateral boundary is indicated by the vertical dashed red arrow (top right) whereas the interspherulitic region ending the spherulite is located in between the inclined red dashed arrows.

Figure 6 focuses on 2D cuts indicating the top views, the tensile direction being normal to the viewgraphs. Figure 6a illustrates the global view at this scale. The essential pattern consisted of a void (in black) surrounded by a polygon, with sometimes stripes linking the central void to the sides of the polygon. By recognizing this pattern, about 40 spherulites were identified in this magnified view. The details of about 10 spherulites are showed in fig. 6b. According to the size of the central void, the stripes assumed to be the crystalline and amorphous lammellae could be distinguished: the smaller the voids, the more discernible the lammellae. Recall that smaller voids were located close to the nucleus for the polar fans microstructures. The details of each of the four labelled spherulites (Sph) in fig. 6b can be summarized as follows:

- Sph #1: the centre is in grey light without any void meaning that the horizontal cut is through the nucleus which is more dense. The lammellae linking the nucleus and the polygonal boundary of this spherulite are visible;
- Sph #2: the centre is also in the dense nucleus, the stripes are visible from the nucleus to the boundaries. In the bottom left boundary of this spherulite (8 o'clock), a void can be observed. At this location; it is probably either an equatorial void or an inter-spherulitic void (or together both);
- Sph #3: the centre is composed of a small void that is at the beginning of a polar fan, so rather closer to a nucleus basis. The lamellae and an inter-spherulitic void (7 o'clock) are also visible ;
- Sph #4: the centre is composed of a large cluster of voids. The lammellae cannot be distinguished. Clearly, the horizontal cut was done at the end of a polar fan (close to the inter-spherulitic matter).

Given the above mentioned resolution of the polygons of spherulite' boundaries, the top views will be used for the measurement of the diameters of the deformed spherulites.

4.2 Analysis of spherulites inside the VOIs'

So as to obtain the maximum number of spherulites and taking advantage of the patterns recognized from the nano-tomography, the analyses were carried out on the three data sets with the resolution corresponding to $1 \text{ px} = 0.7 \text{ }\mu\text{m}$.

Figure 7 focuses on 2D cuts showing the top views of the three VOIs'. Figure 7a displays again the reconstructed tomographic images of the three VOIs'. In figure 7b, more than 300 recognized polygonal boundaries of deformed spherulites were manually identified. It can be noticed that only spherulites in the core could be treated. The cylindrical coordinates were recalled in the bottom of the figure. For each identified spherulite, two perpendicular diameters were measured, respectively along r and θ directions.

Similar to figure 7, figure 8 focuses on the side views of the three VOIs'. This time, figure 8a showing again the reconstructed tomographic images has already been used for the determination of the heights of the deformed spherulites, by referring to the polar fans in [Laiarinandrasana et al., 2016a]. Drawings of the boundaries of the deformed spherulites in each VOI were operated in figure 8b. Only the spherulites in the cores were taken into considerations. Due to the high interlacing of the deformed spherulites from these views, an average of 50 deformed spherulites were utilized for the heights measurement, along the z direction in the cylindrical coordinates.

4.3 Histograms of characteristic lengths of deformed spherulites

Figure 9 focuses on the diameters measured on the deformed spherulites in the three VOIs'. The numbers of the identified spherulites explored were displayed in the ordinates of the histograms. The columns a) and b) correspond to the r and θ -diameters respectively. The mean value of the diameter together with the number of the prescribed VOI were indicated within each histogram. For each VOI, r and θ -diameters were observed to be similar: the deformed spherulites exhibited, at least, transverse isotropy. Moreover, the

closer to the maximum necked region (minimum thickness), the lower the value of the spherulite diameter. Note also that although the histograms are not at the same scale, the mean diameters are shared by less and less deformed spherulites in respectively VOI#1, VOI#2 and VOI#3. In other words, the histograms are “more flat” in VOI#1 than in VOI#3; or the statistical mode value is more distinct in VOI#3 than in VOI#1.

The same analysis was performed on the height of the deformed spherulites in figure 10, focusing on the side views. This time, only one histogram was plotted for each VOIs’ based on the height of the polar fans (z -direction) as mentioned above. Again, the histogram is “more flat” in VOI#1 than in VOI#3. The mean values of the height continuously increase from VOI#1 to VOI#3.

4.4 Elongations measurements

Once the average values of the spherulite diameter, the thickness and the height corresponding to each VOI obtained, this subsection attempts to determine the elongations for each VOI. Three scales were then considered, consisting of: the spherulitic, the core and the macroscopic (named as skin). For the two first scales, each VOI was assumed to be the RVE where the calculated elongation was supposed to be homogeneous.

The values determined for each VOI will be assigned to its barycentre.

Table 1: Estimated or measured gauge lengths

| Lengths (μm) | Spherulite | | Core | | Skin | |
|---------------------------|---------------|-------------|----------------|------------|----------------|------------|
| | Avg. diameter | Avg. height | Min. thickness | VOI height | Min. thickness | VOI height |
| VOI #1-2 | 56 | 56 | 1300 | 784 | 2000 | 784 |
| VOI #3 | 56 | 56 | 1300 | 672 | 2000 | 672 |

Gauge lengths at three scales The gauge length being required for the determination of the elongations, table 1 summarizes it for each VOI and at each scale. The material is assumed to be isotropic, only two elongations were considered: a longitudinal one corresponding to the height and a transverse one attributed to the spherulite diameter and the minimum (at mid-width) thickness for the core and the skin VOI.

It should be mentioned that:

- For the spherulites: due to a good initial circularity (sphericity), for the three VOIs’, the two directions have similar gauge length, equal to the average spherulite diameter (56 μm);
- For the core VOIs: as mentioned in subsection 2.1. the initial thickness is equal to 1300 μm . Concerning the initial height, the number of deformed spherulites in Fig. 8b along a vertical line was determined for each VOI. The result was 14 and 12 for respectively VOI#1-2 and VOI#3. The “average” initial height was obtained by multiplying the latter numbers by 56 μm ;
- For the skin VOIs: as mentioned in subsection 2.1. the initial thickness is equal to 2000 μm . The same initial height as for core VOIs’ was selected.

Table 2: Characteristic lengths measured on deformed VOI

| Lengths (μm) | Spherulite | | Core | | Skin | |
|---------------------------|---------------|-------------|----------------|------------|----------------|------------|
| | Avg. diameter | Avg. height | Min. thickness | VOI height | Min. thickness | VOI height |
| VOI #1 | 48 | 99 | 814.8 | 1430 | 1386 | 1430 |
| VOI #2 | 45 | 112 | 709.8 | 1430 | 1214 | 1430 |
| VOI #3 | 27.5 | 132 | 637 | 1331 | 1110 | 1331 |

Measured characteristic lengths : Table 2 displays the measurement of various specific lengths from deformed VOI. Due to large deformation measured, the elongation, defined as the ratio of the deformed length related to the initial length, was selected for each VOI. As mentioned above, irreversible deformations were measured. For the sake of simplicity, the subscript p (for plastic or irreversible phenomenon) will not appear in the following on the elongation.

From Tables 1 and 2, the longitudinal $\lambda_L \geq 1$ and transverse $\lambda_T \leq 1$ were introduced so as to plot their evolution along the z -position of the three VOIs (Fig. 11). The deformation of the skin obtained at the surface is the same as that measured by classical experimental techniques such as extensometer or digital

image correlation. Then, the assumption commonly used is the homogeneity of the deformation through the thickness. Checking this homogeneity is one of the originality of the present work.

Evolution of the longitudinal elongations Fig. 11 shows the evolution of the longitudinal elongation λ_L from the bottom of the neck (less necked region = VOI#1) to the most pronounced necked region VOI#3.

By construction, the longitudinal displacements of both skin and core were similar, giving the same spatial evolution of λ_L (red square and black circle symbols). The equality between the skin and core λ_L obtained here means that 3D imaging technique could not detect slipping at the skin–core interface, which was not well resolved.

A continuous increase of this longitudinal elongation is observed: slight from VOI#1 to VOI#2 but more significant from VOI#2 to VOI#3. About the deformation at the spherulitic level, the increase is quite linear with a steeper slope. Note that, for VOI#1, λ_L was approximately the same for the three scales of analysis. At this location -near the non necked zone- the deformation can be considered as homogeneous through the thickness. Conversely, for VOI#2 and #3, λ_L in the central part (mid-thickness) is higher than those of the core and the skin. The more critical the necking (VOI#3), the bigger the difference between the λ_L at the surface and in the centre.

The ratio between the longitudinal elongation at the surface and at the scale of the spherulite starts at 1 (in VOI#1) then increases to 1.1 (in VOI#2) and reaches 1.2 (in VOI#3). It can be concluded that a heterogeneity in elongation was highlighted in the necked zone. The gradient of λ_L is the highest where the necking is the most critical along the necked zone. The amplification of the elongations was estimated to be in the range of [1, 1.2]. In terms of logarithmic true strain, the magnification went from 1 to 1.15 and ending up to 1.25.

Evolution of the transverse elongations The following discussion holds for tensile tests *i.e.* $\lambda_L \geq 1$. The corresponding transverse elongation λ_T allows the analysis of the so-called Poisson's effect at the three scales of observation. In terms of elongation $\lambda_T \leq 1$ for negative deformation during longitudinal tensile loading. For isotropic materials, the value of λ_T allows the comparison with the Poisson's ratio ν in small deformation. Indeed, the true logarithmic strain being defined as $\ln(\lambda)$,

$$\nu = -\frac{\ln(\lambda_T)}{\ln(\lambda_L)} \quad (18)$$

Accordingly,

- the incompressibility constraint set by $\nu \approx 0.5$ corresponds to $\lambda_T \approx \frac{1}{\sqrt{\lambda_L}}$;
- if $\frac{1}{\sqrt{\lambda_L}} \leq \lambda_T$, then $\nu \leq 0.5$;
- else if $\frac{1}{\sqrt{\lambda_L}} > \lambda_T$, then $\nu > 0.5$.

With these considerations, fig. 12 plots the measured transverse elongations together with the line corresponding to $\frac{1}{\sqrt{\lambda_L}}$ for the sake of comparison.

Figure 12a analyzes λ_T data at the mesoscopic scale (say skin and core). By opposition to λ_L (fig. 11) the measurements at the skin (surface) differed from that at the core, obtained by 3D-imaging. Both λ_T were below $\frac{1}{\sqrt{\lambda_L}}$ curve for all VOIs' all along the necked region. At the surface and at the interface between skin and core regions, $\nu \geq 0.5$.

The average transverse elongation of spherulites was plotted in fig. 12b and compared with $\frac{1}{\sqrt{\lambda_L}}$ curve (black triangle and solid line). In contrast with the aforementioned results at macroscopic scale, here, both VOI#1 and VOI#2 exhibited $\lambda_T \geq \frac{1}{\sqrt{\lambda_L}}$. Only VOI#3 showed an accordance with the observation at macroscopic scale, *i.e.* $\frac{1}{\sqrt{\lambda_L}} \geq \lambda_T$.

These key results are of prime importance to set a discussion about the difference of volume change between the macroscopic (at the surface) and the spherulitic scales.

Evolution of the volume change For large strain formulation, the volume change is given by the Jacobian of the transformation J . By assuming isotropy of the material, the elongations through the width and the thickness are supposed to be equal to λ_T . Therefore, J theoretically reads:

$$J = \frac{V}{V_0} = \lambda_L \times \lambda_T^2 \quad (19)$$

In virtue of eq. 18, J is equal to unity in the case of zero volume change ($\nu = 0.5$) which is commonly denoted as an incompressibility constraint of the material.

$J \geq 1$ or equivalently $\lambda_T \geq \frac{1}{\sqrt{\lambda_L}}$ or $\nu \leq 0.5$ means a volume increase, due to a significant longitudinal extension without “sufficient” lateral contraction. By contrast, $J \leq 1$ ($\lambda_T \leq \frac{1}{\sqrt{\lambda_L}}$ or $\nu \geq 0.5$) corresponds to a volume loss due to too large contraction in comparison with the lateral extension. These comments are valid under tensile loading in the longitudinal direction. In the case of compressive loading in the same longitudinal direction, there is a volume decrease ($J \leq 1$) and the volume increase corresponds to $J \geq 1$.

The above mentioned volume decrease under tensile loading, denoted also as “compaction” or “densification” of the material, has been reported in the literature when Digital Image Correlation (DIC) technique was more and more used [Gaucher-Miri et al., 1997, Cangémi et al., 2004, Addiego et al., 2006, Ponçot et al., 2013].

At the microscopic scale, [Xiong et al., 2018] reported the same phenomena (volume increase or loss) depending on the location considered in the spherulite, that is in equatorial or polar region.

Fig. 13 illustrates the calculated volume change, using eq. 19, along the longitudinal path on the necked region. The horizontal line at $J = 1$ symbolizes the incompressibility constraint, *i.e.* no volume change.

It can be observed that both skin and core exhibited a volume decrease along the necked region from VOI#1 to VOI#3. By contrast, the volume related to the spherulites was observed to increase except from VOI#3. These observations highlighted a strong heterogeneity in the volume change through the thickness, depending on the degree of necking. The measurement at the surface showed an apparent compaction all along the necked region. So far, the determination of the volumetric deformation was carried out by integrating the volume change using the measurement at the surface and assuming its homogeneity through the thickness. These above mentioned observations showed that this approach is highly questionable.

Focusing on the measurement at the spherulitic scale (blue open triangle symbols in fig. 13), a volume increase (positive volumetric deformation) could be measured on VOI #1 and VOI #2. Whereas the amount of this volume increase diminished from VOI #1 to VOI #2, it completely switched into a volume loss (negative volumetric deformation) in VOI #3.

In the next section, a discussion about the micro-mechanisms inducing the nature of volume change is set. Additionally, the consequences of these results on the so-called “intrinsic” stress-strain curves are highlighted.

5 Discussions

5.1 Micro-mechanisms of deformation and voiding inducing volume change

It should be recalled that when semi-crystalline polymers have experienced yielding during tensile tests, microstructural changes were reported to occur [Blaise et al., 2010, Ovalle et al., 2021]. The observations of the microstructure changes were performed when the specimen is stress free. Therefore the observed deformation is irreversible. Attention is paid here on the appearance of polar fans [Pawlak and Galeski, 2008, Pawlak and Galeski, 2010, Selles et al., 2017] like in figs. 4, 5 and 8. Whereas the polar fans were reported to develop inside a spherulite, their characterization in terms of size, morphology and dispersion was studied [Laiarinandrasana et al., 2016b, Laiarinandrasana et al., 2016a]:

- on a volume of interest larger than the size of one spherulite. Typically, voids were reported to be cylindrical and their volume fraction exhibited a gradient showing a maximum located in the centre of the specimen;
- with increasing deformation involving a change in the neck shape. The growth of initially penny shaped voids was described as follows:
 - during the stress-softening stage, the height increased without any change in the diameter;
 - at the beginning of the stress plateau until failure, the height is still increasing but the diameter diminishes. This latter is due to void coalescence in both radial and in column directions [Laiarinandrasana et al., 2016b]. At the end of this process, one can observe the collapse of many cylindrical voids;
 - before the failure, the diameter is stabilized (complete collapse of the voids) the evolution of the height can no longer be observed.

In addition to polar fans development, equatorial dispersed voids appeared during the stress-softening [Selles et al., 2017]. Their specificity was to keep penny shape morphology, exhibiting rather radial extension and even coalescence, and not much increase in height.

In the light of the above mentioned mechanisms, the evolution of voids in the three VOIs’ will be assumed to follow the same trend as for increasing deformation. The “model spherulite” in VOI#1 and VOI#2 will be supposed to experience the same void growth mechanisms as those occurring during the stress softening (appearance and gradual extension of the necking at the surface). VOI#3 is corresponding to the plateau where the necked matter far from the shoulders is stabilized in lateral displacement, while the neck is still extending longitudinally.

At the spherulitic scale, the volume increase in VOI#1 and VOI#2 is then ascribed to the void appearance and growth in the beginning of the necking. Although the void nucleation depends on the resolution of the technique, [Selles et al., 2017] reported for Polyamide 6 that the first appearance of voids under nano-tomography corresponded to the peak stress. At this very beginning of the stress softening, the amount of voids induces volume increase due to:

- a longitudinal “over-extension” caused by the height of these cavities, added to the local extension of left matter in between the penny shaped voids. The longitudinal elongation λ_L combines these two contributions;
- a lateral expansion due to void appearance compensated by the contraction caused by both Poisson’s effect and shrinkage exerted by the skin around. The transverse elongation λ_T is therefore limited and may not reach $1/\sqrt{\lambda_L}$ corresponding to the incompressibility condition.

For VOI#3 where a volume loss was observed at the spherulitic scale, the “over-contraction” is attributed to the above mentioned collapse of cylindrical cavities, once the height is large enough, in addition to the Poisson and skin shrinkage cumulative effects (see for VOI#1 and VOI#2). At this stage (fig. 5b) the so-called “fragmentation of crystalline lamellae” due to large longitudinal extension induces thinner and less numerous lamellae. Once the collapse of voids is complete, meaning a closure of the elongated voids, λ_T can no longer evolve.

Note that, in fig. 13 the volume increase of the spherulite is observed to slow down from VOI#1 to VOI#2. It can be attributed to that VOI#2 contains spherulites that already started the process of void collapse.

At the macroscopic scale, the compaction is observed for both skin and core and for all VOIs’. However, the skin showed less volume loss than the core, with a constant difference in λ_T of about 0.08 all along the VOIs’. At the scale of the core, the contraction is due to that of all spherulites inside the VOI together with the deformation of the extended left matrix. The larger the void, the more the negative volumetric deformation due to their collapse. The volume loss in coarse spherulites is greater than that in small ones.

The skin, composed of much more smaller spherulites can deform by rolling of the spherulites each other provoking a “flow” of the overall material. It shrinks less than the core with coarse spherulites. Additionally, the material flow as mentioned above, operates so as to induce warping of the cross section of the specimen. The measurement being carried out at mid-width, that is, at the minimum thickness of the material, enhances the compaction with regards to the given extension. The core material, is subjected to the “over-contraction” of the skin together with partial collapse of voids inside.

5.2 Consequence on the true strain and true stress

The concept of RVE considers homogeneity of the continuum medium as well as the stress and strain tensors within. While the RVE at the macroscopic scale (skin and core) were described in subsection 3.2, that of the spherulite is to be defined. Actually, this RVE was assumed to be that of the core composed of several spherulites, where the average elongations were measured.

The above results, available in the necked region specific to irreversible deformation, highlighted many kinds of heterogeneity :

- longitudinal due to the thickness/width variation along the z -position of the spherulite RVE;
- lateral due to: i) the skin-core effects; ii) the gradient of void volume fraction where the maximum is located in the centre.

In figs. 11 and 12b, the plastic deformation gradient of the spherulitic RVE can be written using $\lambda_r = \lambda_\theta = \lambda_T$ and $\lambda_z = \lambda_L$. Therefore, for each VOI, \underline{F}^P was completely obtained:

$$\underline{F}^P = \begin{pmatrix} \lambda_T^p & 0 & 0 \\ 0 & \lambda_T^p & 0 \\ 0 & 0 & \lambda_L^p \end{pmatrix} \quad (20)$$

The true plastic strain tensor from eq. (7) can be fully determined as follows:

$$\underline{\varepsilon}^p = \begin{pmatrix} \ln(J^{-1/3}\lambda_T^p) & 0 & 0 \\ 0 & \ln(J^{-1/3}\lambda_T^p) & 0 \\ 0 & 0 & \ln(J^{-1/3}\lambda_L^p) \end{pmatrix} + \begin{pmatrix} \ln(J^p) & 0 & 0 \\ 0 & \ln(J^p) & 0 \\ 0 & 0 & \ln(J^p) \end{pmatrix} \quad (21)$$

$$\text{with } J^p = \left(\frac{V}{V_0}\right)^p = \lambda_L^p (\lambda_T^p)^2$$

This complete true strain tensor, determined experimentally, constituted one of the main results of this work at the spherulitic scale. Equation 21 shows that the strain tensor was splitted into its deviatoric and volumetric parts respectively. The volumetric strain, called also “plastic dilation” [Ognedal et al., 2014] in

the sense that it is irreversible, can be essentially related to the void growth. This latter was quantified and published by [Laiarinandrasana et al., 2016b] for the same sample. The complementary deviatoric part represents the shear strain exerted on the matrix.

Focusing on the volumetric part, fig. 13 clearly shows that apart from VOI#1 and VOI#2 at the spherulite scale, the other VOIs exhibited negative volumetric strain under tensile direction. This compaction *i.e.* $\nu > 0.5$ cannot be approached by the classical continuum mechanics. Therefore, these cases will not be further discussed. The deformation gradient or strain tensors for the two selected VOIs' can be considered as the inputs to obtain the complete stress tensors. Two approaches can then be identified to apply the continuum mechanics:

- an average spherulite considered as a homogenized porous medium, the cross section being that of the core VOI;
- a spherulite consisting of a mix of ideally dense matrix containing an amount of pores which can be converted to void volume fraction (porosity).

In both approaches, as the deformation gradient does not exhibit the incompressibility constraint, the stress tensor is expected to be triaxial: the transverse stresses are not null. Due to the gradients and the 3D effects, only constitutive models relating the strain tensor to the stress tensor, should be utilized. The use of finite element (FE) code provided with reliable model is then recommended. Thanks to the measured load, the only known stress is the axial component of the first Piola Kirschhoff (engineering) stress tensor $\tilde{\Pi}$:

$$\Pi_L = \frac{F}{S_0} \quad (22)$$

where F is the load, S_0 is the initial area of the cross section of the core RVE. The experimental results required constitutive models which handle the hydrostatic pressure (isostatic stress) with respect to the volume change. Note that a "simple" von Mises criterion fails to account for this phenomenon. Once the appropriate model is identified, the optimization of material parameters is based on F/S_0 value so as to calibrate the simulated Π_L .

Π_T can then be accessed but it depends on the sensitivity of the model to the stress triaxiality *i.e.* the isostatic stress. By returning eq. (17), the Cauchy (true) stress tensor can be deduced:

$$\tilde{\sigma} = \frac{1}{J} \tilde{\Pi} \tilde{F}^T \quad (23)$$

giving:

$$\tilde{\sigma} = \begin{pmatrix} \frac{\Pi_T}{\lambda_L \lambda_T} & 0 & 0 \\ 0 & \frac{\Pi_T}{\lambda_L \lambda_T} & 0 \\ 0 & 0 & \frac{\Pi_L}{\lambda_T^2} \end{pmatrix} \quad (24)$$

Before the yield stress, that is in the (visco)elastic part of the stress-strain curve, both macroscopic and spherulitic RVE's fulfill the conditions of homogeneity. However, attention should be paid on the use of the true stress σ_L and the true strain $\ln(\lambda_L)$ to derive the elastic coefficients like Young's modulus or the Poisson's ratio. Beyond the yield stress *i.e.* during the necking process, depending on the chosen model, the true stress-strain curve should be plotted using the maximum principal stress σ_L in eq. (24). Attention should be paid on the transverse stresses which are not null, conversely to the uniaxial case assumed in the classical stress-strain curve. These investigations are required when working on the local true stresses at the scale of the spherulites.

5.3 Towards AI analysis: deep learning of deformed spherulite morphology

In this work, figs. 5-6 allowed the recognition of the shape and the mechanisms of voiding within several spherulites. The top and side views of these spherulites were utilized so as to learn about the characteristic patterns when they were deformed and voided.

The knowledge of the patterns enabled to identify the deformed spherulites in figs. 7-8, followed by the plotting of the histograms in figs. 9-10. All these time consuming operations were executed by eyes and by hand. The numbers of analyzed spherulites were specified in these latter figures (figs. 9-10: about 50 and 300 in the side and top views, respectively). These numbers were of course fewer than the total number of spherulites in the tomography data sets.

From the authors' viewpoint, these valuable data were not completely exploited. One of the aim of this paper was then to give a route for machine learning approach. The first task consisting of the identification the spherulite patterns in fully 3D, was detailed in this paper. Based on this knowledge, a machine learning routine should allow the production of more elements in the histograms from big data sets. Furthermore, other spherulitic microstructures coming from other thermoplastics are available in the laboratory to do so.

6 Conclusion

This work focused on an isotactic polypropylene: a semi-crystalline thermoplastic with spherulitic microstructure that exhibited a skin-core effects. Three experimental volumes of interest (VOI) were introduced:

- the skin VOI including the free surface, where common laboratory measurements could be carried out;
- the core VOI where the cross section remained rectangular during the deformation and within which several spherulites could be observed in their deformation process;
- the VOI at the spherulitic scale constituted by the same core VOI but where the evolution of characteristic lengths of the spherulites could be measured all along the shape of the necked region.

For each of the three VOIs, an attempt was made to determine the complete deformation gradient tensor composed of both isochoric and volumetric components. Attention was especially paid to the transverse elongation so as to analyze the volume change. None of the VOIs' showed the commonly admitted isochoric assumption, corresponding to the quasi-incompressibility constraint. Conversely, most of them turned out to exhibit volume loss (compaction) of the material at an advanced stage of the necking process. Only two VOIs, located in the neck shoulder (equivalent to the beginning of the necking process during a tensile test) showed a volume increase. This latter was ascribed to void nucleation due to the own architecture of the spherulites. The consecutive growth of these voids arranged in columns (polar fans) was then shown when the necking process progressed. The compaction of the VOI was attributed to the collapse of extended cylindrical shaped voids in the deformed polar fans. Thanks to the measurements of average changes in the height and diameter of the spherulites, the complete deformation gradient of the VOIs' could be determined beyond the yield stress. Especially the volume increase at the beginning of the necking process made the classical "isochoric" plasticity theory questionable. Therefore, a route was proposed to obtain the local true stress tensor in the framework of continuum mechanics under finite strain formulation. The plastic dilation was accounted for in such kind of modelling dedicated for finite element analysis.

7 FIGURES

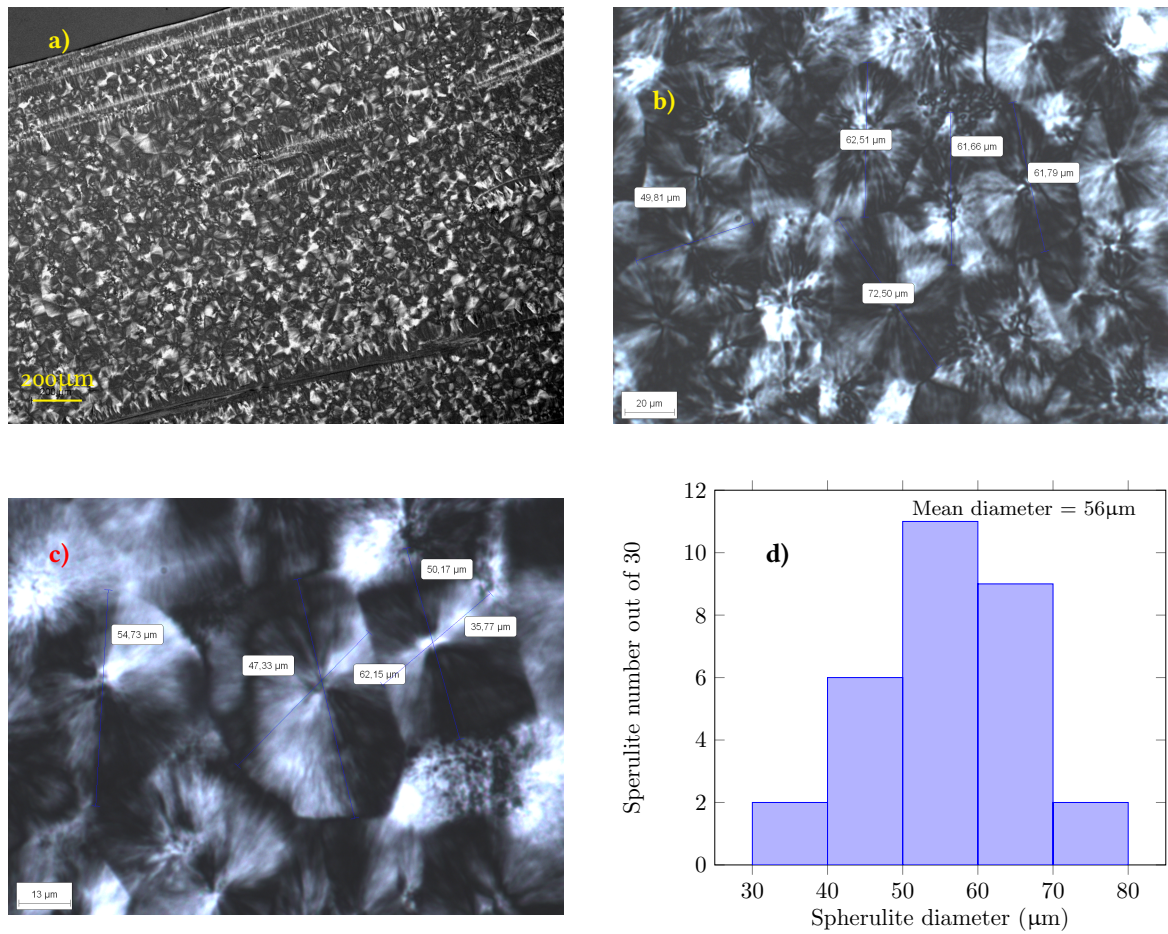


Figure 1: Optical microscopy examination of the spherulites on microtomed thin film of the PP under study: a) Large surface; b) and c) Focuses on smaller surfaces to allow diameter measurements; d) Histogram of the spherulite diameter measured on 30 net spherulites

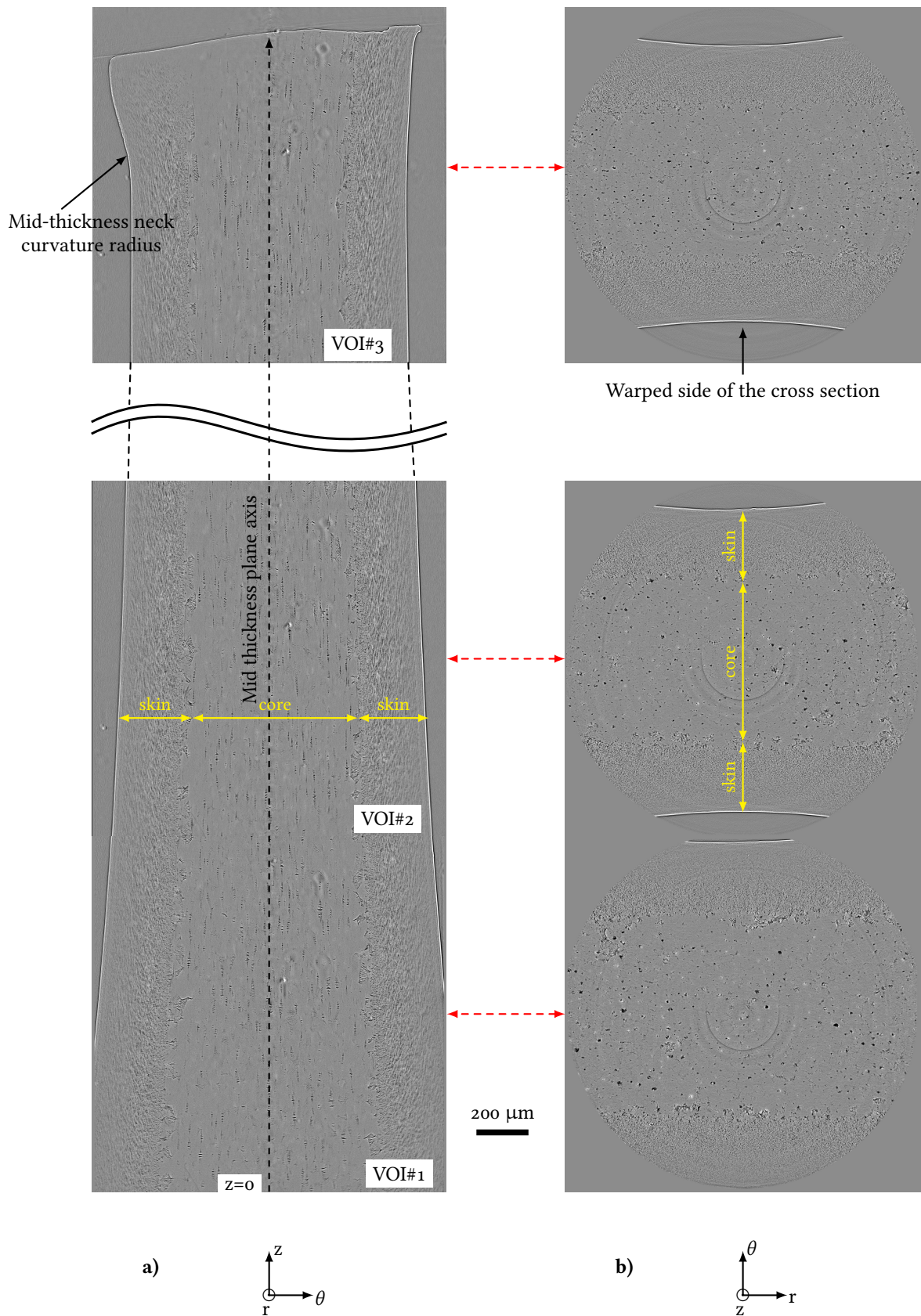


Figure 2: The three microtomography data sets representative of the Volumes of interest (VOI): a) Side views at mid-width cuts; b) Corresponding top views of respective VOIs'. Yellow arrows indicate the core/skin regions allowing their thicknesses to be measured

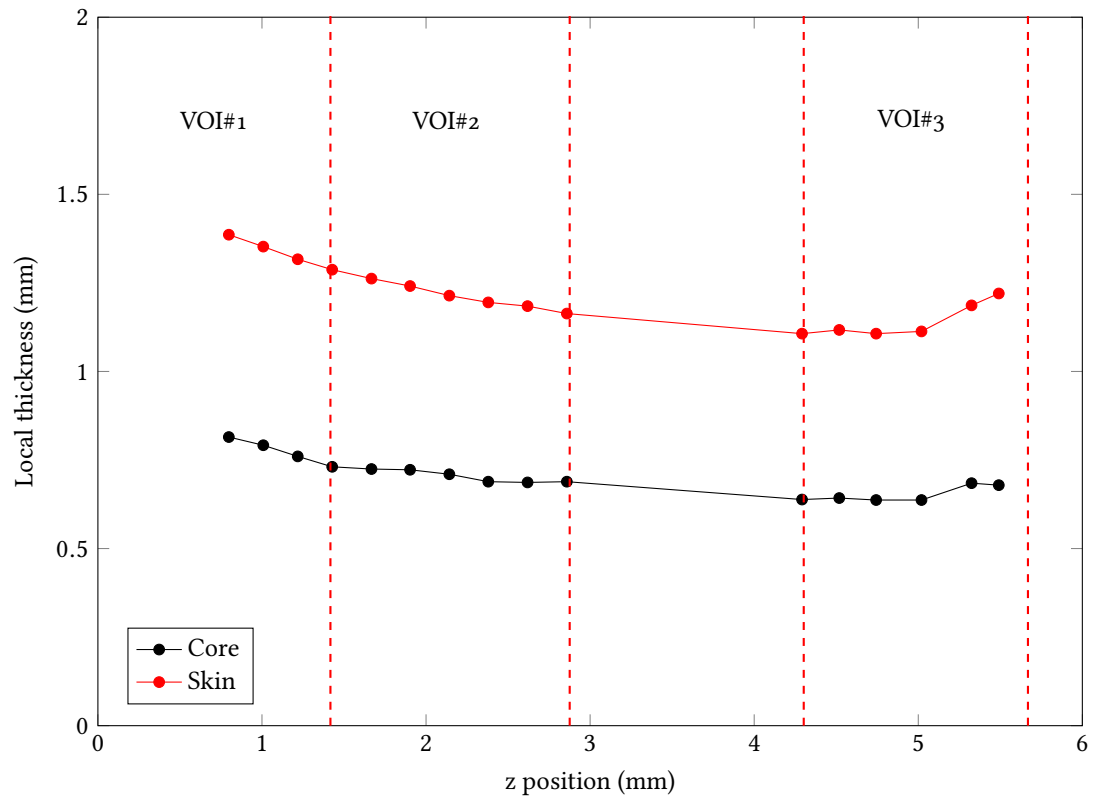


Figure 3: Profiles of the core and skin according to z . Relative position and characteristic heights of the VOIs'

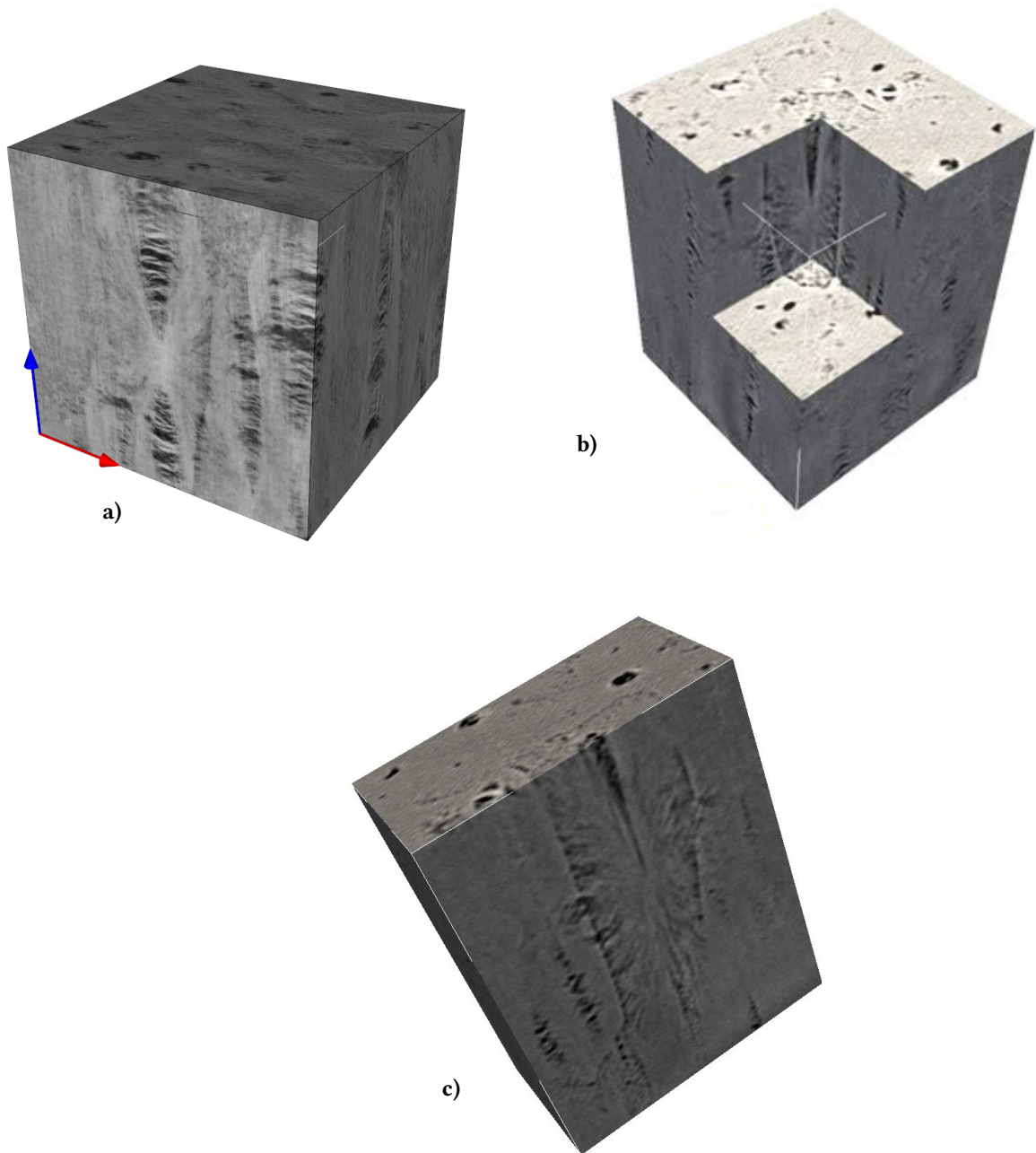


Figure 4: Various 3D views of deformed spherulites showing polar fans, from data sets obtained from synchrotron radiation tomography with a resolution corresponding to 1 pixel size $\approx 0.7\mu\text{m}$. *Cube side about 140 μm*

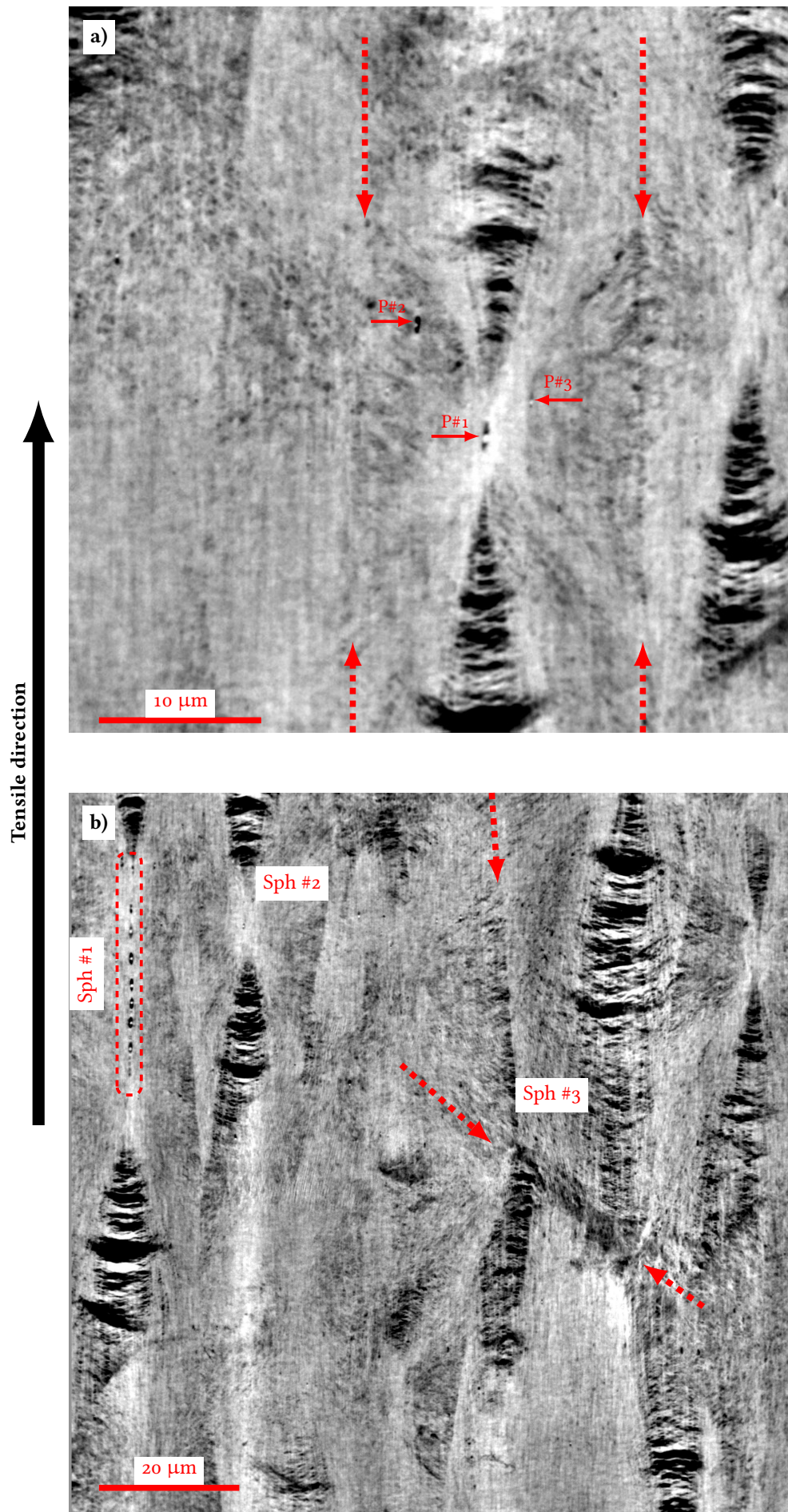


Figure 5: Side views of data set of deformed PP at a resolution of 50 nm: a) detailed view of a couple of polar fans; b) global view 102 μm x 102 μm.

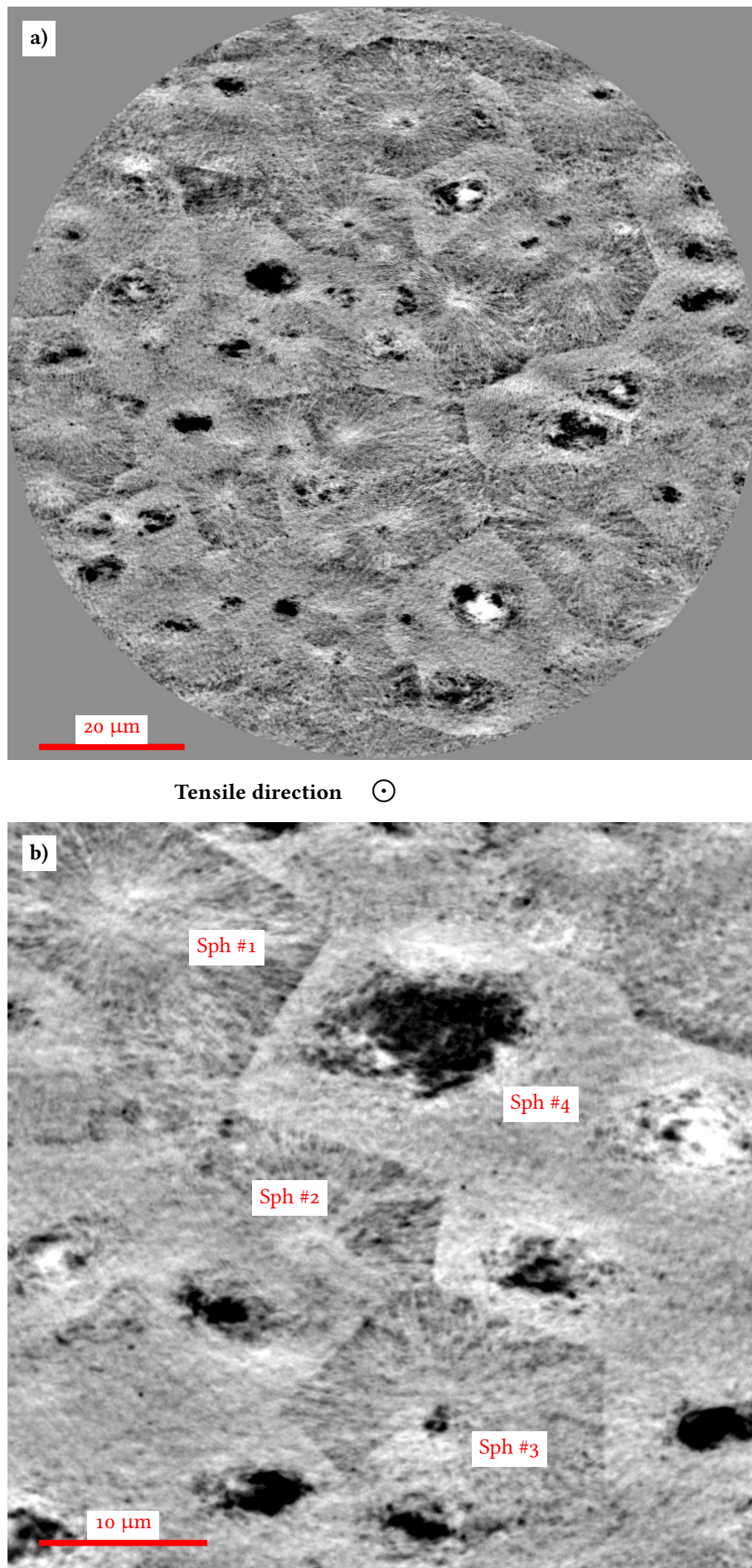


Figure 6: Top views of data set of deformed PP at a resolution of 50 nm: a) global view 102 μm x 102 μm; b) closer look at few spherulites: 45 μm x 45 μm

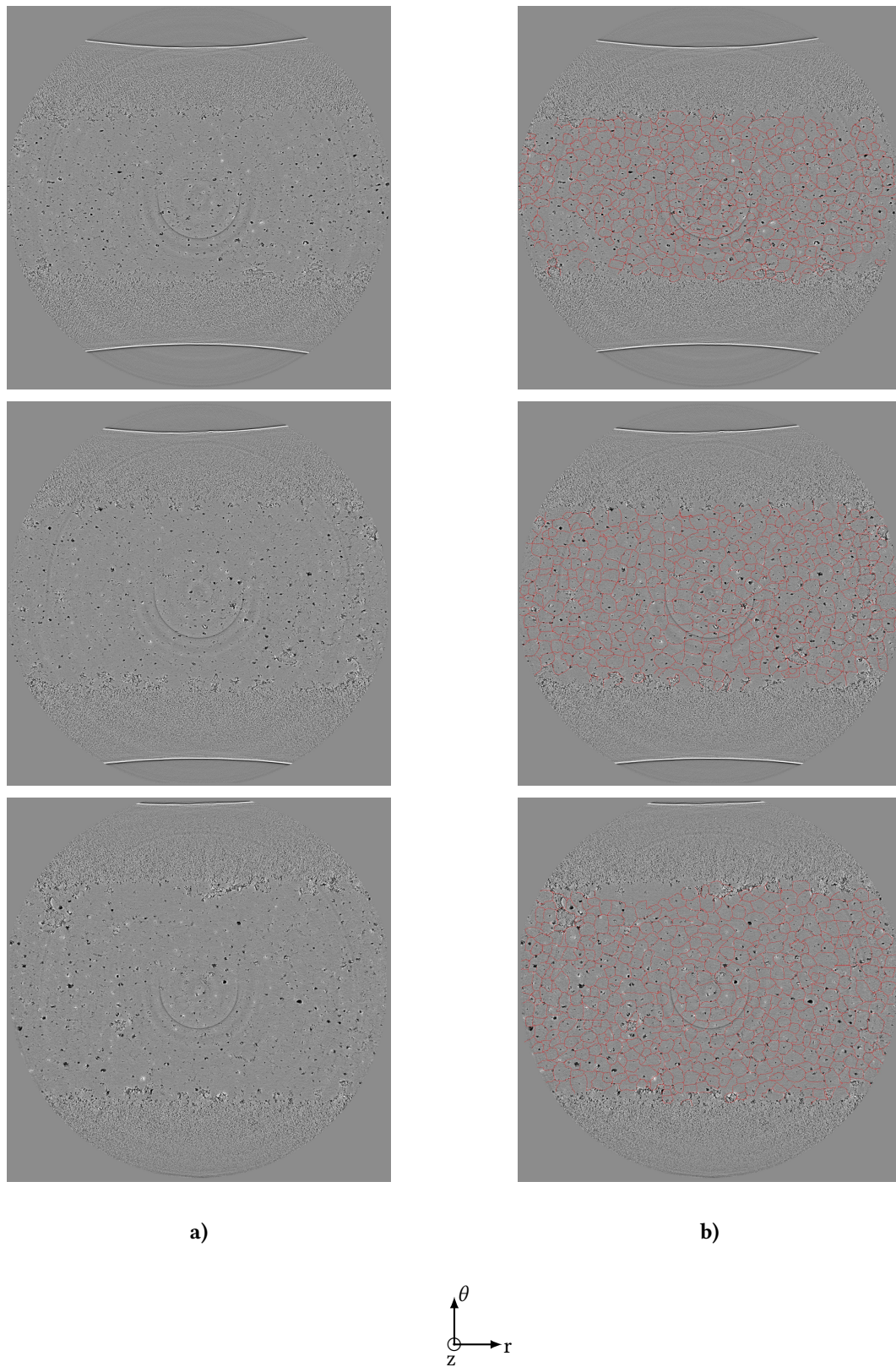


Figure 7: 2D section top views of microtomography data of the three VOIs' presented in fig. 2 so as to determine the diameters of the deformed spherulites: a) Reconstructed images; b) drawings of the identified boundaries for the deformed spherulites

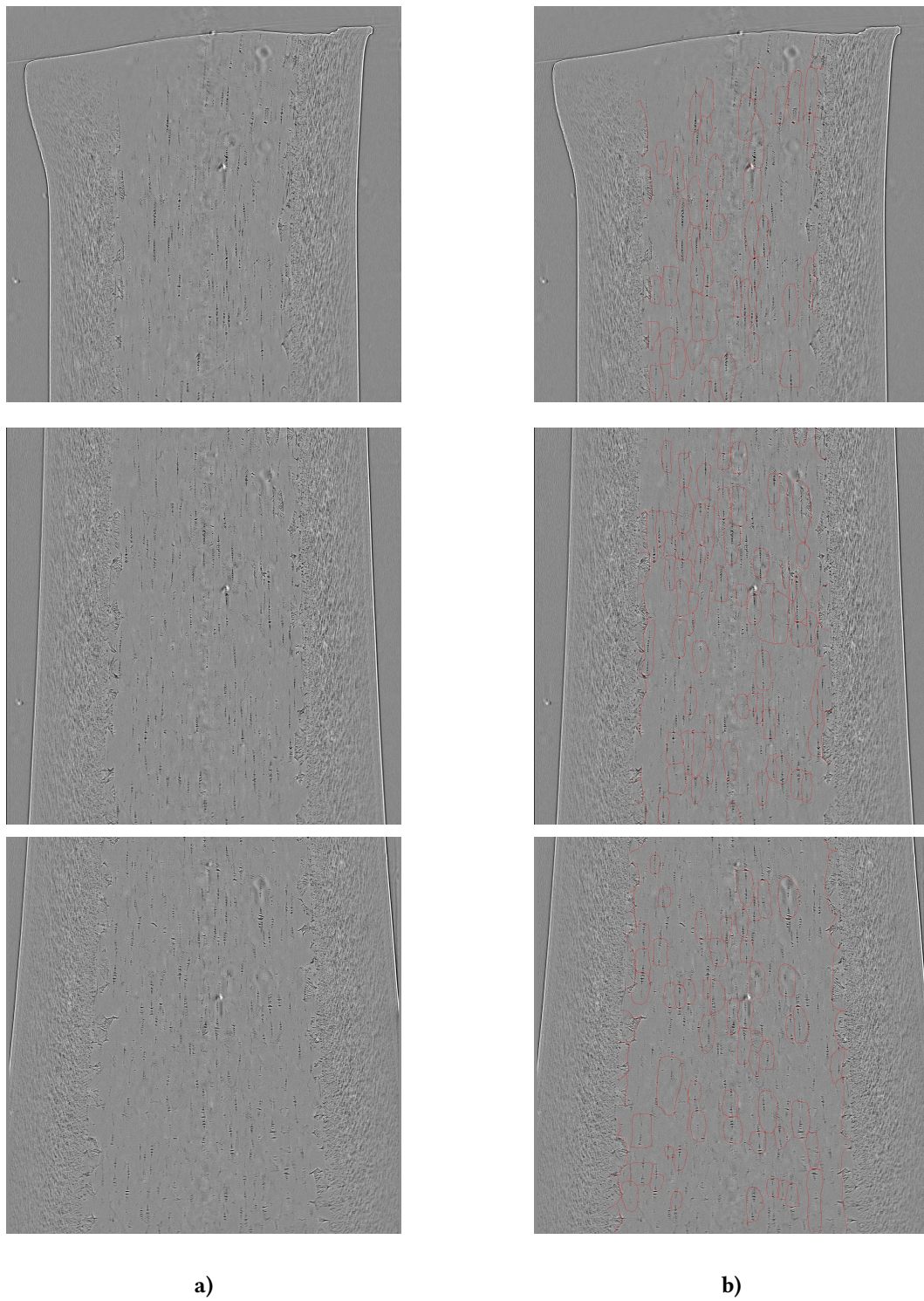


Figure 8: Side views of the three VOIs' presented in fig. 2 so as to determine the heights of the deformed spherulites: a) Reconstructed images; b) drawings of the identified polar fans inside the deformed spherulites

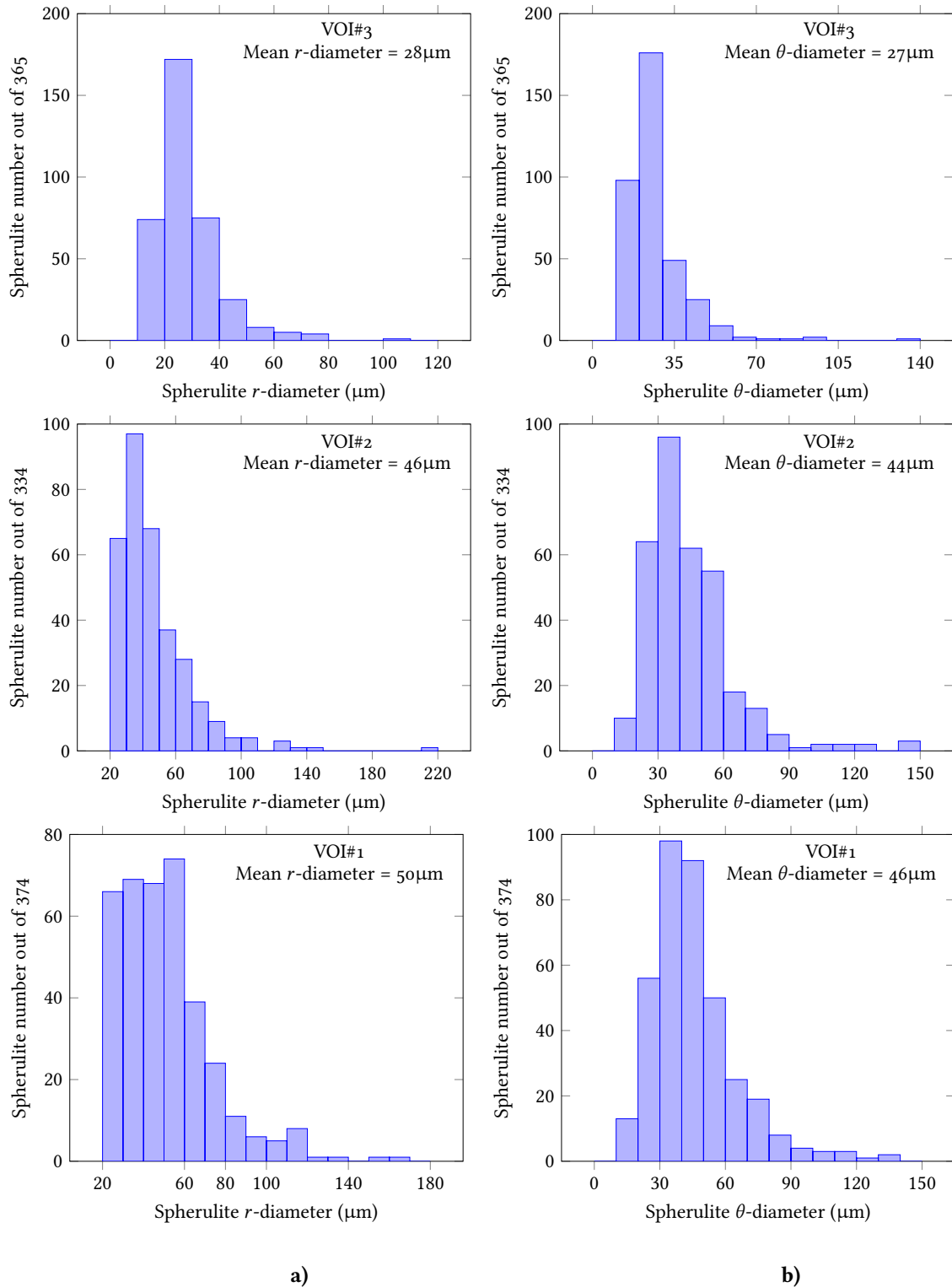


Figure 9: Histograms of the diameters of the identified deformed spherulites in the core, for VOIs' #1,2,3 from bottom to top: a) diameter along r -direction; b) diameter along θ -direction (See fig. 7 for the cylindrical coordinates).

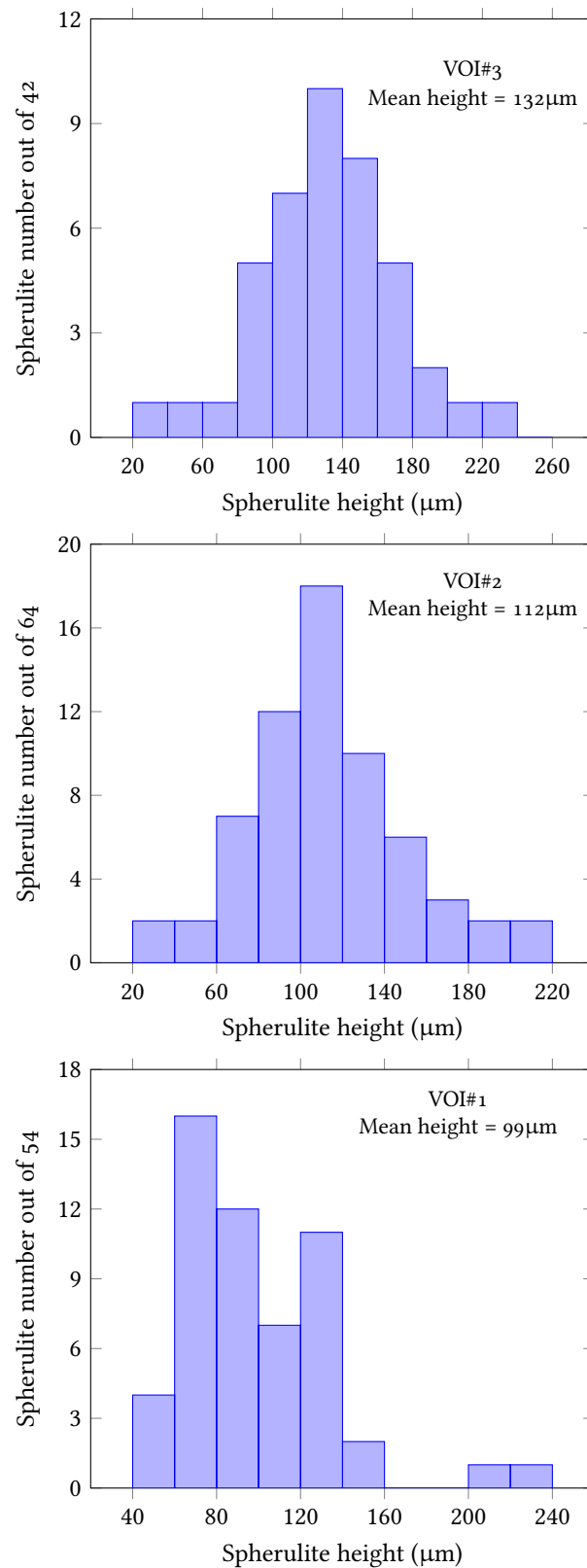


Figure 10: Histograms of the heights of the identified polar fans in the core along the z-direction, for VOIs' #1,2,3 from bottom to top.

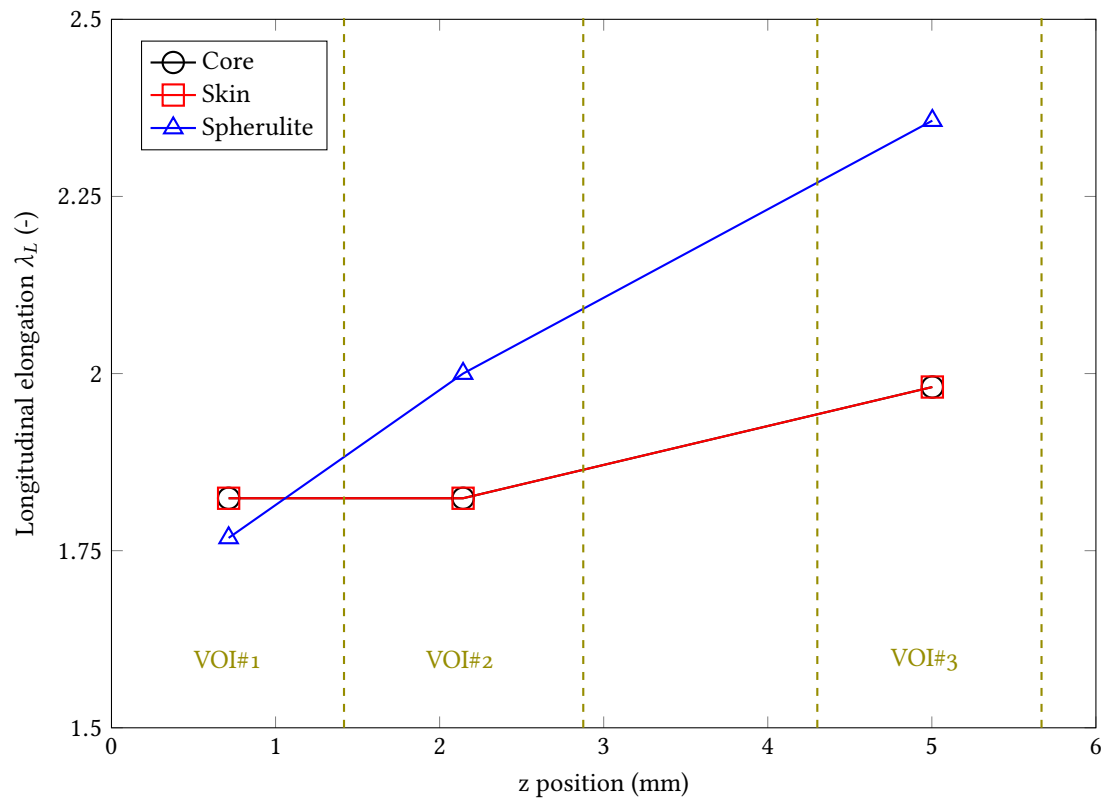


Figure 11: Evolution of the longitudinal elongations (λ_L) along the necked region

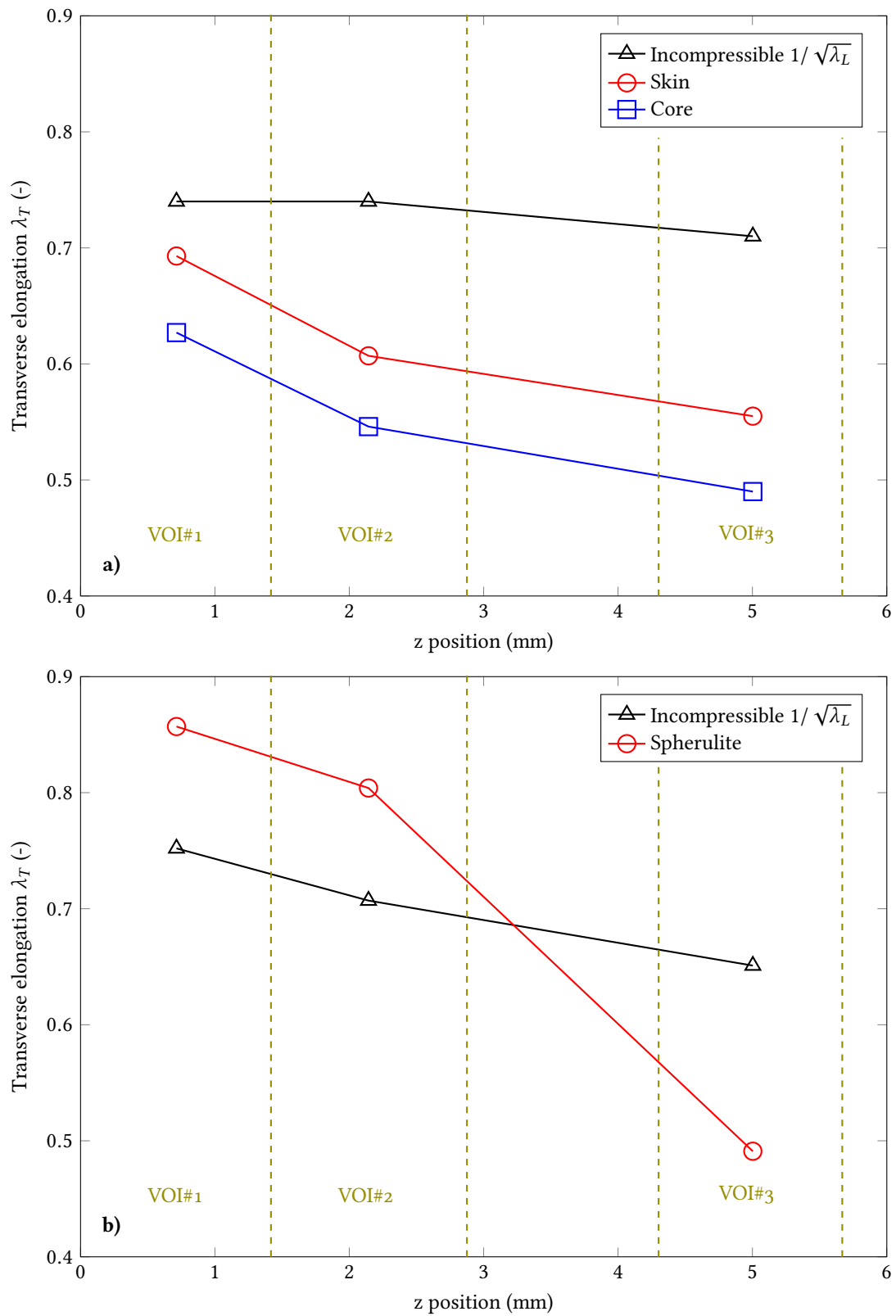


Figure 12: Evolution of the transverse elongations (λ_T) along the necked region: a) Core and skin; b) at the spherulitic scale

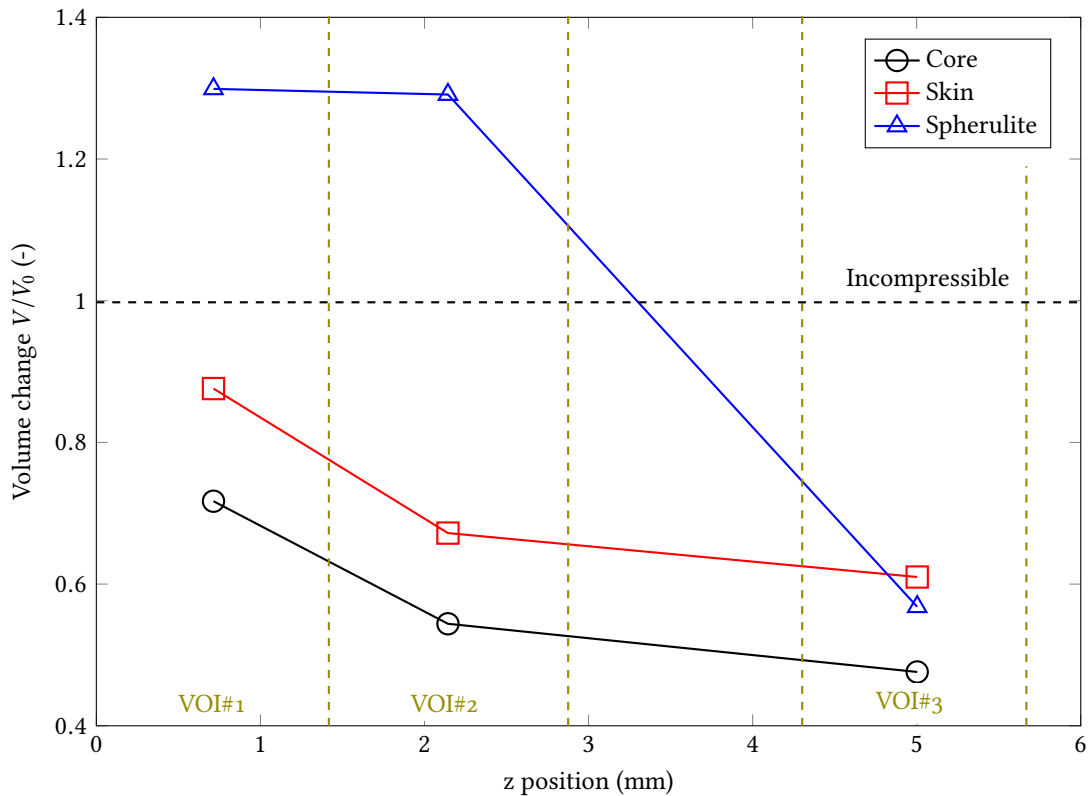


Figure 13: Evolution of the volume change V/V_0 along the necked region

References

- [Addiego et al., 2006] Addiego, F., Dahoun, A., G'Sell, C., and Hiver, J. (2006). Characterization of volume strain at large deformation under uniaxial tension in high-density polyethylene. *Polymer*, 47(12):4387–4399.
- [Assouline et al., 2001] Assouline, E., Wachtel, E., Grigull, S., Lustiger, A., Wagner, H., and Marom, G. (2001). Lamellar twisting in α isotactic polypropylene transcrystallinity investigated by synchrotron microbeam x-ray diffraction. *Polymer*, 42(14):6231–6237.
- [Blaise et al., 2010] Blaise, A., Baravian, C., André, S., Dillet, J., Michot, L., and Mokso, R. (2010). Investigation of the mesostructure of a mechanically deformed hdpe by synchrotron microtomography. *Macromolecules*, 43(19):8143–8152.
- [Cangémi et al., 2004] Cangémi, L., Elkoun, S., G'Sell, C., and Meimon, Y. (2004). Volume strain changes of plasticized poly(vinylidene fluoride) during tensile and creep tests. *Journal of Applied Polymer Science*, 91:1784–1791.
- [Duffo et al., 1995] Duffo, P., Monasse, B., Haudin, J., G'Sell, C., and Dahoun, A. (1995). Rheology of polypropylene in the solid state. *Journal of Materials Science*, 311:701–711.
- [Estevez et al., 2000] Estevez, R., Tijssens, M., and Van der Giessen, E. (2000). Modeling of the competition between shear yielding and crazing in glassy polymers. *Journal of the Mechanics and Physics of Solids*, 48(12):2585–2617.
- [Gaucher-Miri et al., 1997] Gaucher-Miri, V., Depecker, C., and Séguéla, R. (1997). Reversible strain-induced order in the amorphous phase of a low-density ethylene/butene copolymer. *Journal of Polymer Science: Part B: Polymer Physics*, 35:2151–2159.
- [Haudin, 2013] Haudin, J. (2013). *Handbook of polymer crystallization*. E. Piorkowska et G.C. Rutledge, John Wiley & Sons, Inc., Hoboken, New Jersey, USA Dunod.
- [Kantz et al., 1972] Kantz, M. R., Newman Jr., H. D., and Stigale, F. H. (1972). The skin-core morphology and structure–property relationships in injection-molded polypropylene. *Journal of Applied Polymer Science*, 16(5):1249–1260.

- [Laiarinandrasana et al., 2016a] Laiarinandrasana, L., Klinkova, O., Morgeneyer, T., Proudhon, H., Nguyen, F., and Ludwig, W. (2016a). Three dimensional quantification of the anisotropic void evolution in deformed semi-crystalline polyamide 6. *International Journal of Plasticity*, 83:19–36.
- [Laiarinandrasana et al., 2016b] Laiarinandrasana, L., Selles, N., Klinkova, O., Morgeneyer, T., Proudhon, H., and Helfen, L. (2016b). Structural versus microstructural evolution of semi-crystalline polymers during necking under tension: Influence of the skin-core effects, the relative humidity and the strain rate. *Polymer Testing*, 55:297–309.
- [Morgeneyer et al., 2014] Morgeneyer, T. F., Proudhon, H., Cloetens, P., Ludwig, W., Roirand, Q., Laiarinandrasana, L., and Maire, E. (2014). Nanovoid morphology and distribution in deformed hdpe studied by magnified synchrotron radiation holotomography. *Polymer*, 55(25):6439–6443.
- [Ognedal et al., 2014] Ognedal, A. S., Clausen, A. H., Dahlen, A., and Hopperstad, O. S. (2014). Behavior of pvc and hdpe under highly triaxial stress states: An experimental and numerical study. *Mechanics of Materials*, 72:94–108.
- [Ovalle et al., 2021] Ovalle, C., Cloetens, P., Proudhon, H., Morgeneyer, T., and Laiarinandrasana, L. (2021). Nanocavitation mechanisms in deformed high density polyethylene(hdpe) using synchrotron radiation nanotomography. *Polymer*, 229:123959.
- [Pawlak and Galeski, 2008] Pawlak, A. and Galeski, A. (2008). Cavitation during tensile deformation of polypropylene. *Macromolecules*, 41:2839 – 2851.
- [Pawlak and Galeski, 2010] Pawlak, A. and Galeski, A. (2010). Cavitation and morphological changes in polypropylene deformed at elevated temperatures. *Journal of Polymer Science: Part B: Polymer Physics*, 48:1271 – 1280.
- [Ponçot et al., 2013] Ponçot, M., Addiego, F., and Dahoun, A. (2013). True intrinsic mechanical behaviour of semi-crystalline and amorphous polymers: Influences of volume deformation and cavities shape. *International Journal of Plasticity*, 40:126–139.
- [Raphael et al., 2019] Raphael, I., SAINTIER, N., Robert, G., Béga, J., and Laiarinandrasana, L. (2019). On the role of the spherulitic microstructure in fatigue damage of pure polymer and glass-fiber reinforced semi-crystalline polyamide 6.6. *International Journal of Fatigue*, 126:44–54.
- [Rozanski and Galeski, 2013] Rozanski, A. and Galeski, A. (2013). Plastic yielding of semicrystalline polymers affected by amorphous phase. *Int. J. Plasticity*, 41:14 – 29.
- [Selles et al., 2017] Selles, N., Cloetens, P., Proudhon, H., Morgeneyer, T., Klinkova, O., Saintier, N., and Laiarinandrasana, L. (2017). Voiding mechanisms in deformed polyamide 6 observed at the nanometric scale. *Macromolecules*, 50(11):4372–4383.
- [Séguéla, 2007] Séguéla, R. (2007). On the natural draw ratio of semi-crystalline polymers: Review of the mechanical, physical and molecular aspects/rheology of polypropylene in the solid state. *Macromolecular Materials and Engineering*, 292:235–244.
- [van Dommelen et al., 2003] van Dommelen, J., Parks, D., Boyce, M., Brekelmans, W., and Baaijens, F. (2003). Micromechanical modeling of the elasto-viscoplastic behavior of semi-crystalline polymers. *Journal of the Mechanics and Physics of Solids*, 51(3):519–541.
- [Ward, 1971] Ward, I. (1971). Review: The yield behaviour of polymers. *Journal of Materials Science*, 6:1397–1417.
- [Xiong et al., 2013] Xiong, B., Lame, O., Chenal, J., Rochas, C., Séguéla, R., and Vigier, G. (2013). In-situ saxs study and modeling of cavitation/crystal-shear competition in semi-crystalline polymers: influence of temperature and microstructure in polyethylene. *Polymer*, 54:5408–5418.
- [Xiong et al., 2018] Xiong, B., Lame, O., Seguela, R., and Men, Y. (2018). Micro/macro-stress relationship and local stress distribution in polyethylene spherulites upon uniaxial stretching in the small strain domain. *Polymer*, 140:215–224.